Materials Characterization 225 (2025) 115104

Contents lists available at ScienceDirect

Materials Characterization

journal homepage: www.elsevier.com/locate/matchar

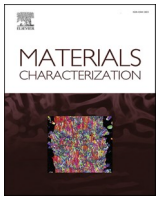

New fire-resistant steel alloyed with Nb-Mo-B-Ti: Mechanical properties and characterization via SEM, TEM, and APT

L.F. Bauri [a,*], A.M. Ferreira [a], E.A. Ariza-Echeverri [a,b], F.M.S.B. Carvalho [a,c], P.M.C.D. Gomes [a], R. Sonkusare [d], Y. Lu [d], T. Boll [d], A.P. Tschiptschin [a], H. Goldenstein [a]

[a] Universidade de São Paulo, Escola Politécnica, Departamento de Engenharia Metalúrgica e de Materiais, São Paulo, SP, Brazil
[b] Grupo de Nuevos Materiales, Facultad de Ingeniería, Universidad del Magdalena, Santa Marta, Colombia
[c] Instituto de Pesquisas Tecnológicas (IPT), São Paulo, SP, Brazil
[d] Karlsruhe Institute of Technology, Institute for Applied Materials (IAM-WK), Institute of Nanotechnology (INT), Karlsruhe Nano Micro Facility (KNMFi), Karlsruhe, KA, Germany

ARTICLE INFO

Keywords:
Fire-resistant steels
Fire simulation test
NbC nanoprecipitates

ABSTRACT

Fire-Resistant Steels (FRS) are widely used to ensure building stability during fire incidents, enabling safe evacuation. In this study, a FRS alloyed with Nb, Mo, B, and Ti was cast, thermomechanically processed, and air-cooled to achieve the "as received" condition. The yield strength (YS) was evaluated through tensile tests at room temperature (YS RT) and at 600 °C (YS 600 °C), along with a constant pre-load test at high temperatures. A Fire-Simulation (FS) test was subsequently conducted using a quenching dilatometer. Thermodynamic analysis, Scanning Electron Microscopy (SEM), Transmission Electron Microscopy (TEM), and Atom Probe Tomography (APT) were used to characterize the samples. The tensile tests revealed a YS ratio $\frac{YS(600^{\circ}C)}{YS\ RT}$ of 0.76, exceeding the requirement set by the Japanese Code. TEM analysis identified (Nb, Ti, Mo)C precipitates ≈ 20 nm in the as-received condition, consistent with thermodynamic predictions. After the fire simulation test, additional (Nb, Ti)C carbides ≈ 10 nm were observed. APT revealed that Nb and C atoms were aligned along dislocations or subgrain structures under simulated fire condition, whereas these atoms were sparsely distributed in the as-received condition. The formation of NbC nanoprecipitates, influenced by the presence of Mo, Ti, and B atoms, provides valuable insights into the enhancement of fire-resistant materials.

1. Introduction

Following the World Trade Center terrorist attack in 2001, several studies have explored the enhancement of Fire-Resistant Steels (FRS) through thermomechanical controlled processing (TMCP) and optimized chemical compositions [1–5]. Under fire conditions, these FRS must exhibit yield strengths at 600 °C ($YS_{600°C}$) that are at least two-thirds of their yield strength at room temperature [6–9]. While molybdenum (Mo) microalloyed FRS are commercially available, their high cost limits their widespread use in building construction. This has prompted research into alternative alloying elements, such as niobium (Nb) and boron (B), to achieve similar or superior performance in FRS.

Ferreira et al. [10] investigated the effects of adding B and Nb to two low-carbon steels (0.10 wt% Nb + 28 ppm B and 0.10 wt% Nb without B) using ab initio calculations based on density functional theory (DFT) and high-temperature mechanical testing. Their findings revealed that the combination of B and Nb reduces the energy of vacancy formation, suggesting a synergistic effect that retards vacancy diffusion.

Escobar et al. [11] examined a commercial FRS (Fe - 0.13C – 0.11Cr – 0.38Mo – 0.04 V, wt%) by evaluating the kinetics of microstructural degradation during fire simulation conditions using dilatometric tests and in situ synchrotron X-ray diffraction. They concluded that ferrite and pearlite microstructures remained more stable during fire simulation, whereas bainite and martensite, being more metastable, exhibited lower stability.

The degradation of mechanical properties under fire conditions is primarily attributed to several mechanisms, including dislocation mobility [12], microstructural instabilities [11], precipitates coarsening [9,13], and grain boundaries sliding (creeping effects) [9,13–15]. Recent studies suggest that solute-vacancy interactions can also influence dislocation mobility at elevated temperatures [8,10]. Alloying elements such as Mo, Nb, and Cr are commonly used in FRS due to their

* Corresponding author.
E-mail address: luizbauri@usp.br (L.F. Bauri).

https://doi.org/10.1016/j.matchar.2025.115104
Received 22 July 2024; Received in revised form 27 April 2025; Accepted 28 April 2025
Available online 8 May 2025

beneficial effects on microstructure, which contribute to hardening through: a) the precipitation of secondary nanocarbides [3,4,8]; b) the formation of high-dislocation-density complex acicular microstructures [16]; c) and c) solid solution strengthening [17].

In this context, the present work aims to investigate a new fire-resistant steel alloyed with Nb, B, and Ti, with a reduced Mo content compared to previous studies [8,11,18,19] and the industrial practices [8,11,18,19]. The study focuses on evaluating the mechanical properties and microstructural characteristics of the alloy before and after fire simulation tests.

2. Experimental procedure

An 80 kg ingot was cast in a vacuum induction melting furnace (VIM) to produce an ingot with a thickness of 80 mm. After that, the ingot was cut and hot rolled with a Thermomechanical Controlled Process (TMCP) to induce the refinement of the structure. The reheating temperature was ≈ 1260 °C to grant the dissolution of niobium carbides. TMCP was performed with six rolling steps of 76 % total reduction thickness, ending above Ac_3 temperature (≈ 830 °C). After hot rolling, the plate was air-cooled (≈ 0.65 °C/s) to room temperature, denoting the "as-received" condition. The chemical composition of the developed steel is detailed in Table 1. The quantification of substitutional elements was performed using X-ray Fluorescence (XRF), which provides precise measurements of metallic constituents. We utilized inductive coupled Plasma Optical Emission Spectrometry (ICP-OES) for boron. This technique is especially adept at detecting and quantifying low concentrations of boron with high accuracy. Additionally, the levels of carbon were determined using a direct combustion method. This method involves incinerating a sample in an oxygen-rich environment and analyzing the resulting gases to precisely measure these non-metallic elements. To facilitate a direct comparison between these measurements, expressed in weight percent (wt%), and the results from Atom Probe Tomography (APT), which are reported in atomic percent (at.%), conversions were made. These adjustments were based on the relative atomic masses, Avogadro's number, and the stoichiometry of the alloy. This conversion allows for a direct comparison with APT data, which inherently depends on the number of atoms rather than their mass.

The Thermocalc® software was employed using the TCFE9 database and the CALPHAD calculation method to determine the phases formed at thermodynamic equilibrium and their respective chemical compositions in the temperature range between 1200 °C and 600 °C.

Tensile tests at room temperature were conducted following ASTM E8 standard [20], using a Time Groups machine (Model WDW W-100), with a strain rate $\varepsilon = 7{,}3.10^{-4}.s^{-1}$. To determine the YS, a parallel line was drawn with an offset of 0.2 relative to the linear region of the stress-strain curve.

Tensile tests at 600 °C were conducted according to ASTM E21–20 standard [21], using an Instron 2382 machine. The machine has a capacity of 100 kN and a displacement control of 4 mm/min. A split furnace model was used to heat the sample at 10 °C/min (0.17 °C/s). A high-temperature extensometer was employed for data acquisition. The tests were conducted at 600 °C, after a 15 min soak for homogenization of the specimen at the test temperature.

The constant pre-load test involves subjecting the material to a constant loading, varying the test temperature, and under a desired heating rate. This test has been used to simulate laboratory-scale fire conditions [9,16,22]. This study used a heating rate of 5 °C/min (0.08 °C/s), and the maximum test temperature was approximately 800 °C. LVDT DC/DC type extensometer and "S" type thermocouples were used, fixed at the center of the specimen's usable area.

Walp [9] suggests using half of the material's YS at RT for conducting the constant pre-load test. However, in this work a normalized stress of 188 MPa was used, which is the value of half of the YS of the FRS used in Japan and extensively studied by Gomes [22]. Additionally, a temperature failure criterion was adopted, consisting of measuring the temperature when the material reaches 1 % of plastic or permanent deformation [9,16,22].

Fire simulation (FS) at 600 °C, for 30 min, was conducted in a DIL 805 A/D Bahr Dilatometer under high vacuum and Helium-assisted quenching, following ASTM 119–20 [23]. Heating and cooling rates of 2 °C/s and 5 °C/s were used, following Escobar et al.'s recommendations [11].

Scanning Electron Microscopy (FEG-SEM FEI-Inspect F50®) was used for microstructural characterization. For this, metallographic samples were grounded with #100 to #1200 sandpaper, polished with 6 μm, 3 μm, and 1 μm diamond paste, and finished using colloidal silica (0.25 μm). Etching was carried out using Nital 2 % (ethanol +2 % HNO_3).

Transmission Electron Microscopy (TEM) was performed for both conditions. The sample preparation was made using an electropolishing technique. Selected Area Electron Diffraction (SAED - STEM), Bright Field (BF - STEM), and High Angle Annular Dark-Field (HAADF - STEM) configurations were used to obtain the images. The indexing of the diffraction patterns was made using CrysTBox software. Also, Energy-Dispersive X-ray Spectroscopy (EDX) mapping was performed to characterize the chemical composition of the precipitates.

Atom Probe Tomography (Local Electrode Atom Probe, LEAP 4000× HR) was carried out on both as received and fire simulated conditions, using needle-shaped samples extracted using Focused Ion Beam (FIB) in a dual beam scanning electron microscope (AURIGA 60), to identify and characterize the clusters and precipitates not identified via TEM. APT measurements were carried out in laser mode ($\lambda = 355$ nm), with a pulse energy of 50 pJ, pulse frequency of 125 kHz, detection rate of 0.5, and temperature set to 50 K. Integrated Visualization and Analysis Software (IVAS 3.6.14, Cameca) was used to reconstruct the data, obtain atomic maps, and perform cluster analysis.

The analysis detected Gallium at a concentration of approximately 0.15 % in both the as-received and fire-simulated conditions. The occurrence of Ga predominantly at the needle tip is a common characteristic in APT samples prepared using FIB-SEM. During the milling process, Ga ions can implant into the surface layers of the sample, potentially influencing the subsequent material analysis. This presence of Ga is an anticipated artifact stemming from the FIB-SEM preparation, where Ga ions are employed in the ion beam to sculpt the specimen into an appropriate shape for APT analysis. To address and mitigate the impact of Ga contamination on the analytical results, specific measures were implemented. The region where Ga was detected primarily at the top of the needle tip was precisely identified using initial scans. This region was subsequently excluded from the APT data analysis to ensure that the compositional data analyzed and presented reflected the steel's intrinsic characteristics, devoid of any Ga influence.

Table 1
Chemical composition of the FRS steel (wt% and at.%).

Wt% C	Wt% Mn	Wt% Nb	Wt% Mo	Wt% B	Wt% Ti
0.05	1.00	0.10	0.25	0.003	0.014
At.% C	**At.% Mn**	**At.% Nb**	**At.% Mo**	**At.% B**	**At.% Ti**
15.64	68.38	4.04	9.79	1.04	1.10

3. Results

3.1. Mechanical properties

Table 2 presents the results of the average values of Yield Strength (YS), Ultimate Tensile Strength (UTS), and Total Elongation measured at room temperature and at 600 °C. Besides, the ratio between the YS $\frac{YS(600^{\circ}C)}{YS\ RT}$ is shown. The sample exhibited a YS RT of 540 MPa and YS 600 °C of 410 MPa. Meanwhile, the YS ratio reached the value of 0.76. The UTS properties exhibited an UTS RT of 665 MPa and UTS 600 °C of

Table 2
– Average values of Yield Strength (YS), Ultimate Tensile Strength (UTS), and Total Elongation measured at room temperature and at 600 °C, and the ratio between the YS 600 °C/YS RT.

YS (MPa)		UTS (MPa)		Elongation (%)		YS 600 °C/ YS RT
RT	600 °C	RT	600 °C	RT	600 °C	
540 (± 6)	410 (± 1)	665 (± 5)	460 (± 7)	19.2 (± 1.4)	19.8 (± 2.9)	0.76

460 MPa. Moreover, the total elongation values were 19.2 % and 19.8 % at RT and 600 °C, respectively. Finally, Fig. 1 depicts the result of the constant pre-load test compared to FRS literature [10,22]. The sample exhibited a failure temperature of 720 °C.

3.2. Thermodynamic analysis

Fig. 2 illustrates the molar fraction of phases in thermodynamic equilibrium as a function of temperature obtained using the Thermo-calc® software. The main predicted phases included: austenite, ferrite, NbC, Fe_3C, $(Fe, Mo)_3$ (C), and MoC. Additionally, Table 3 provides the chemical compositions of the phases in the temperature range between 1200 °C and 600 °C.

3.3. Scanning electron microscopy (SEM)

Fig. 3 shows the results of the as-received and fire-simulated microstructures obtained by SEM. The as-received condition, Figs. 3(a) and (b) shows austenite-martensite (MA) aggregates at grain boundaries, degenerate pearlite, and primary nanoprecipitates (see yellow arrows) dispersed in a ferritic matrix. The fire-simulated sample, see Figs. 3(c) and (d), showed a similar microstructure, containing additional nano-sized secondary precipitates at subgrains and in the ferrite matrix, some of them aligned.

3.4. Transmission electron microscopy (TEM)

Fig. 4 shows the TEM results for both conditions (as-received and fire-simulated). Figs. 4(a), (b), and (c) show the analysis for the as-received condition, and Figs. 4(d), (e), (f), and (g) are related to the fire-simulated condition. Fig. 4(a) shows the (HAADF - STEM) image, evidencing a small nanoprecipitate (≈ 20 nm) that nucleated during the

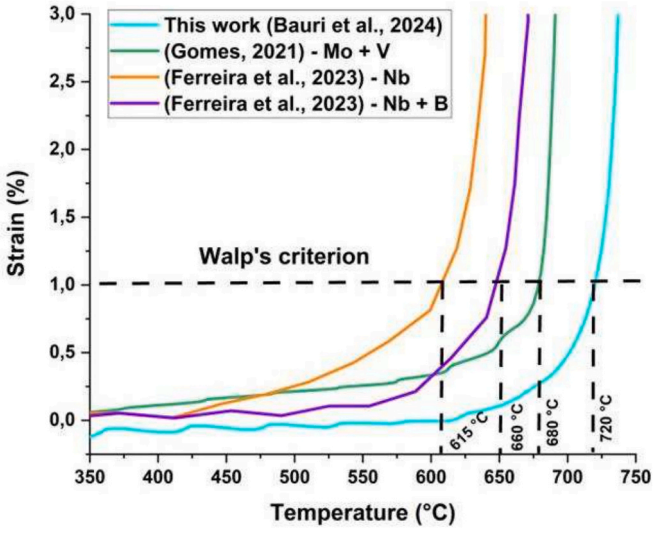

Fig. 1. – Mechanical properties obtained for the FRS. Constant pre-load test compared to FRS literature [10,22].

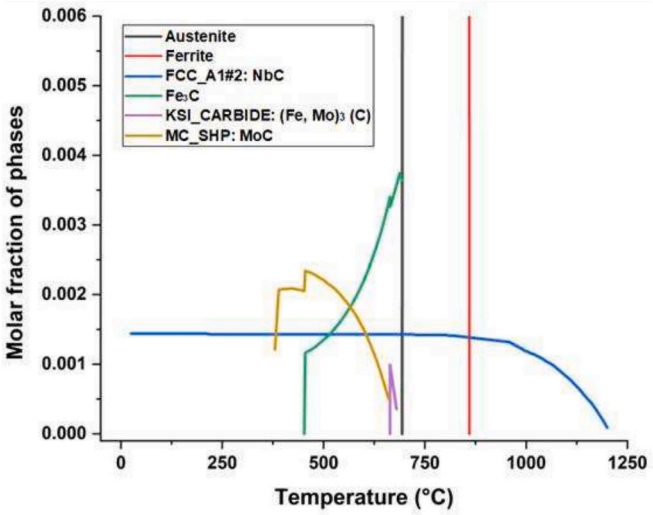

Fig. 2. Thermodynamic analysis obtained using Thermocalc® software.

thermomechanical processing stage (primary nanoprecipitate). The (SAED - STEM) pattern shown in Fig. 4(b) depicts the orientation relationship of the nanoprecipitate related to the ferrite matrix. Still, Fig. 4 (c) depicts the EDX mapping in the same region, evidencing a (Nb, Ti, Mo)C nanoprecipitate type.

Fig. 4(d) presents the (BF - STEM) image of the fire-simulated specimen. In this case, it was possible to observe the presence of nanoprecipitates (≈ 10 nm) inside the ferrite matrix, as indicated by red arrows (secondary precipitates nucleated during fire simulation). The HAADF image (see Fig. 4(e)) shows nanoprecipitates and dislocation structures. Fig. 4(f) presents the (SAED – STEM) patterns of the ferrite matrix and the nanoprecipitate (white circle with black arrow superposed) shown in Fig. 4(e). Fig. 4(g) shows the EDX mapping acquired in the same area as Fig. 4(e), indicating a (Nb, Ti)C-type nanoprecipitate. The EDS results suggest a gradient in Mo concentration within and around the primary NbC nanoprecipitates. Specifically, regions of lower Mo concentration, appearing darker in the EDS maps, were observed centrally within the precipitates, while an increased intensity of Mo seems evident towards the outer contours of these precipitates. This distribution suggests a tendency for Mo to segregate towards the interfaces of the NbC-type nanoprecipitates. This segregation behavior would imply a potential mechanism whereby Mo enhances the refinement of these secondary nanoprecipitates. The interaction between Mo and the NbC precipitates likely contributes to the modification of the precipitate's growth and stability, which is critical under high-temperature conditions experienced during fire simulations.

3.5. Atom probe tomography (APT)

Fig. 5(a) shows that in the small area analyzed in the "as-received" condition, the chemical elements are apparently in solid solution. However, it is important to emphasize that for the initial condition, NbC-type precipitates were observed in the SEM and TEM results. Nevertheless, they were not detected via APT because the selected needle region did not contain these precipitates.

In the "fire-simulated" condition, NbC nanoprecipitates, see Fig. 5 (b), were observed, possibly aligned with dislocations or low-angle grain boundaries, interacting with the Ti, Mo, and B atoms (highlighted in red rectangles). In addition, Fig. 5(c) shows the proxigram result (iso-concentration 1 at. %C) for the fire-simulated condition. For this case, an increase in Mo content was observed inside the NbC nanoprecipitate, with almost equal atomic composition (≈ 5 ± 1 at. %) of each chemical element.

Fig. 6 presents the representative mass-to-charge spectra obtained

Table 3
Chemical compositions of the phases in the temperature range between 1200 °C and 600 °C.

T. (°C)	Stable phases	Molar fraction						
		Nb	Ti	C	Mo	Mn	B	Fe
1200	Austenite	$5{,}50.10^{-4}$	$1{,}60.10^{-4}$	0,002	0,001	0,01	$9{,}00.10^{-5}$	0,99
	FCC_A1#2: NbC	0,34	0,18	0,48	0,0005	$2{,}00.10^{-5}$	$3{,}70.10^{-7}$	–
1000	Austenite	$1{,}00.10^{-4}$	$7{,}27.10^{-6}$	0,0017	0,001	0,01	$9{,}00.10^{-5}$	0,99
	FCC_A1#2: NbC	0,41	0,11	0,48	0,0002	$2{,}00.10^{-5}$	$1{,}21.10^{-8}$	–
800	Austenite	$1{,}04.10^{-6}$	$1{,}04.10^{-7}$	0,007	$8{,}60.10^{-4}$	0,02	$9{,}88.10^{-6}$	0,97
	Ferrite	$1{,}51.10^{-6}$	$1{,}15.10^{-7}$	0,0002	0,001	0,01	$4{,}67.10^{-6}$	0,99
	FCC_A1#2: NbC	0,39	0,11	0,49	0,0001	$1{,}20.10^{-4}$	$1{,}46.10^{-11}$	–
600	Ferrite	$3{,}99.10^{-9}$	$2{,}27.10^{-10}$	$1{,}20.10^{-4}$	$5{,}50.10^{-4}$	0,01	$4{,}57.10^{-8}$	0,99
	FCC_A1#2: NbC	0,38	0,11	0,50	$3{,}00.10^{-5}$	0,002	$5{,}02.10^{-13}$	–
	Fe_3C	$8{,}71.10^{-12}$	–	0,25	0,003	0,16	0,001	0,59
	MC_SHP: MoC	–	–	0,50	0,50	–	–	–

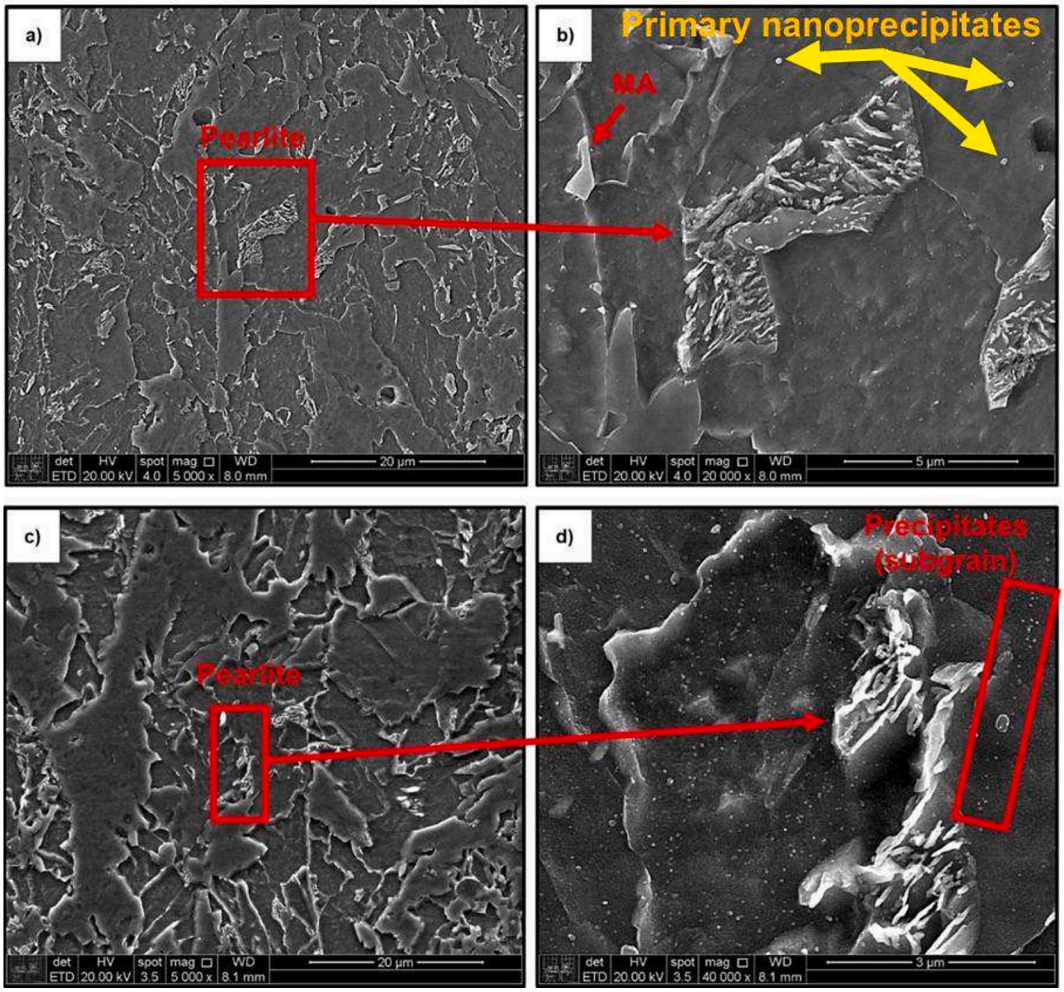

Fig. 3. Microstructural characterization obtained via SEM. (a) and (b) as-received condition; (c) and (d) fire simulated condition.

from APT for both the as-received (Fig. 6(a)) and fire-simulated (Fig. 6 (b)) conditions of the fire-resistant steel. The spectra display the characteristic peaks corresponding to the main elements detected in the material, including Fe, C, Nb, Mo, Ti, B, and trace levels of Ga (from FIB-SEM preparation). All peaks are color-coded for clarity according to the ion species legend provided.

4. Discussion

4.1. Types of microstructures in FRS

This work investigates the influence of the fire simulation test in a FRS concerning its starting microstructure. In the FRS literature [8,9,11,16,24], in the as-received condition, i.e., after TMCP, two types of microstructures with different characteristics are commonly found: acicular microstructures, e.g., bainite, martensite, and MA; and the thermodynamically more stable microstructures, ferrite and pearlite.

For the as-received condition, according to the results obtained via

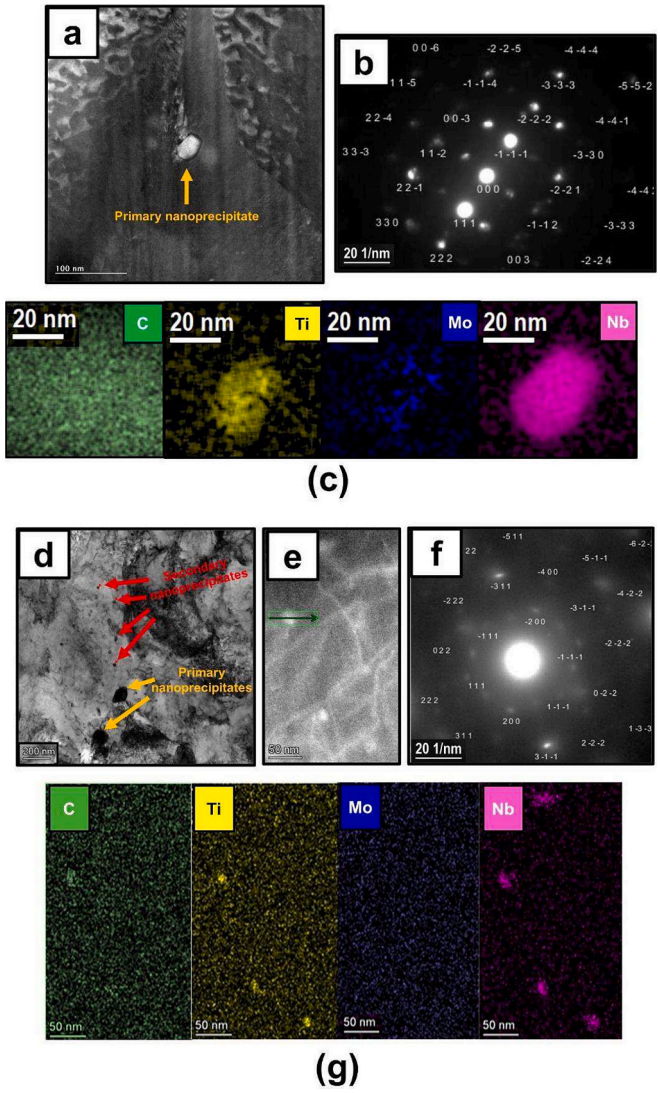

Fig. 4. (a), (b), and (c) as-received condition. (a) HAADF (STEM) image evidencing a primary nanoprecipitate; (b) SAED pattern diffraction related to the nanoprecipitate evidenced in Fig. 4(a); (c) EDS mapping related to the nanoprecipitate shown in Fig. 4(a). Figs. 4(d), (e), (f), and (g) depict the microstructure and chemical composition of the specimen in the fire-simulated condition. (d) BF image showing the nanoprecipitates formed after fire simulation; (e) HAADF (STEM) image evidencing nanoprecipitates and dislocation structures; (f) SAED pattern diffraction related to the nanoprecipitate marked by an arrow in Fig. 4(e); (g) EDS mapping related to the nanoprecipitates shown in Fig. 4(e).

SEM, from Figs. 3(a) and (b), the microstructure is composed of a ferritic matrix + pearlite + MA, containing primary nanoprecipitates formed during the TMCP stage, as predicted by thermodynamic analysis using Thermocalc (see Fig. 2 and Table 3). TEM results and atomic maps showed that the chemical elements are homogeneously distributed in a solid solution in the matrix. Nevertheless, primary nanoprecipitates (Nb, Ti, Mo)C type (≈ 20 nm) were found via TEM (see Fig. 4(a)). Regarding the fire-simulated sample, a few different characteristics were observed concerning the as-received condition, such as: formation of Nb and C solute clusters, secondary nanoprecipitates (Nb, Ti)C type, and MA decomposition.

Escobar et al. [11] described the influence of the kinetics in the microstructural degradation of a FRS from three initial microstructures: (i) ferrite + pearlite; (ii) bainite + retained austenite; (iii) martensite + retained austenite. During fire simulation, it was concluded that ferrite + pearlite remained stable, while metastable microconstituents, such as bainite and martensite, suffered carbon depletion during heating. Nevertheless, bainite proved to be a more stable microconstituent than martensite; its decomposition and cementite precipitation started around 400 °C, while martensite microconstituent began to decompose at 320 °C. Additionally, austenite was the most unstable phase, starting its decomposition at 180 °C. It is important to emphasize that Escobar et al. [11] found only Fe_3C precipitates after fire simulation in a FRS containing Mo and V, which are strong carbide formers.

4.2. Mechanisms improving fire resistance

Even under fire conditions, there are ways to mitigate microstructural degradation. Through the design of TMCP and selecting a suitable chemical composition, it is possible to obtain a microstructure that complies with the minimum requirements of a FRS.

Solid solution hardening occurs when strain fields of solute atoms influence the movement of dislocations. Carbon atoms exert a significant influence on interstitial solid solution hardening in ferrite. Due to their low solubility, there is a tendency for these atoms to segregate towards crystalline defects, such as dislocations or grain boundaries, hindering the mechanisms of plastic deformation.

Moon et al. [16] studied the effects of Mo and Nb addition in FRS and demonstrated that the alloy with the highest Mo content had higher yield strength, due to bainite formation in the starting microstructure. In addition, they showed that during fire simulation, there was a retarding effect in the annihilation of dislocations, due to Mo atoms being in a solid solution, and precipitation of refined carbides MC-type (where M = Ti and Nb).

A substitutional solid solution depends on the difference between the size of the solute atom and the Fe atoms [25]. Jo et al. [8] reported that Mo and Nb atoms largely distort the lattice, causing substitutional solid solution hardening, thus favoring the dislocation annihilation delay at fire temperatures. Ferreira et al. [10] showed that adding B can also decrease the energy of vacancy formation by 11.7 % compared to a purely ferritic material. Additionally, the combination between B + Nb can reduce the energy up to 33.2 %, suggesting that both elements can work in synergy to increase the mechanical strength at high temperatures via a “pinning effect”, consequently retarding vacancy diffusion.

APT results revealed that a portion of the Mo atoms is present in solid solution within the ferritic matrix after the Fire Simulation (FS) test. However, when analyzing the region by EDS near and within the nanoprecipitate, an increase in the Mo content inside the nanoprecipitate was observed, suggesting a tendency for Mo to interact with NbC-type nanoprecipitates and indicating a possible mechanism for refining the secondary nanoprecipitate, which could be responsible for the enhanced fire resistance of the studied steel. This is reflected in the ratio $\frac{YS(600^{\circ}C)}{YS\ RT}$ of 0.76, exceeding the requirements of 0.66 specified in the literature [11,14,18,29] and based on the ASTM A1077/A1077M standard and the Japanese code regulated by the Japanese Industrial Standard (JIS). According to Chijiiwa et al. [18], Mo atoms segregate at the interface of the ferrite matrix and the NbC nanoprecipitates, hindering precipitate growth at high temperatures. Furthermore, some authors highlight the main effects of Mo on FRS: solid solution hardening [8,17,26]; hardenability increasing (promoting the formation of acicular microstructures) [16,17]; recovery and recrystallization delay [17]; synergistic effect between Mo and Nb [8,27], which can modify the precipitation sequence and increase the yield strength. For these reasons, it is essential to emphasize its relevance in FRS.

The literature reveals a scarcity of studies on the effects of B in FRS. However, a recent study by Ferreira et al. [28] investigated the influence of B in FRS. The chemical composition of the alloy examined in that study is similar to the one studied in the present work, differing only by the absence of Mo. Using TEM and APT techniques, combined with analyses of the alloy’s mechanical properties, the authors concluded that

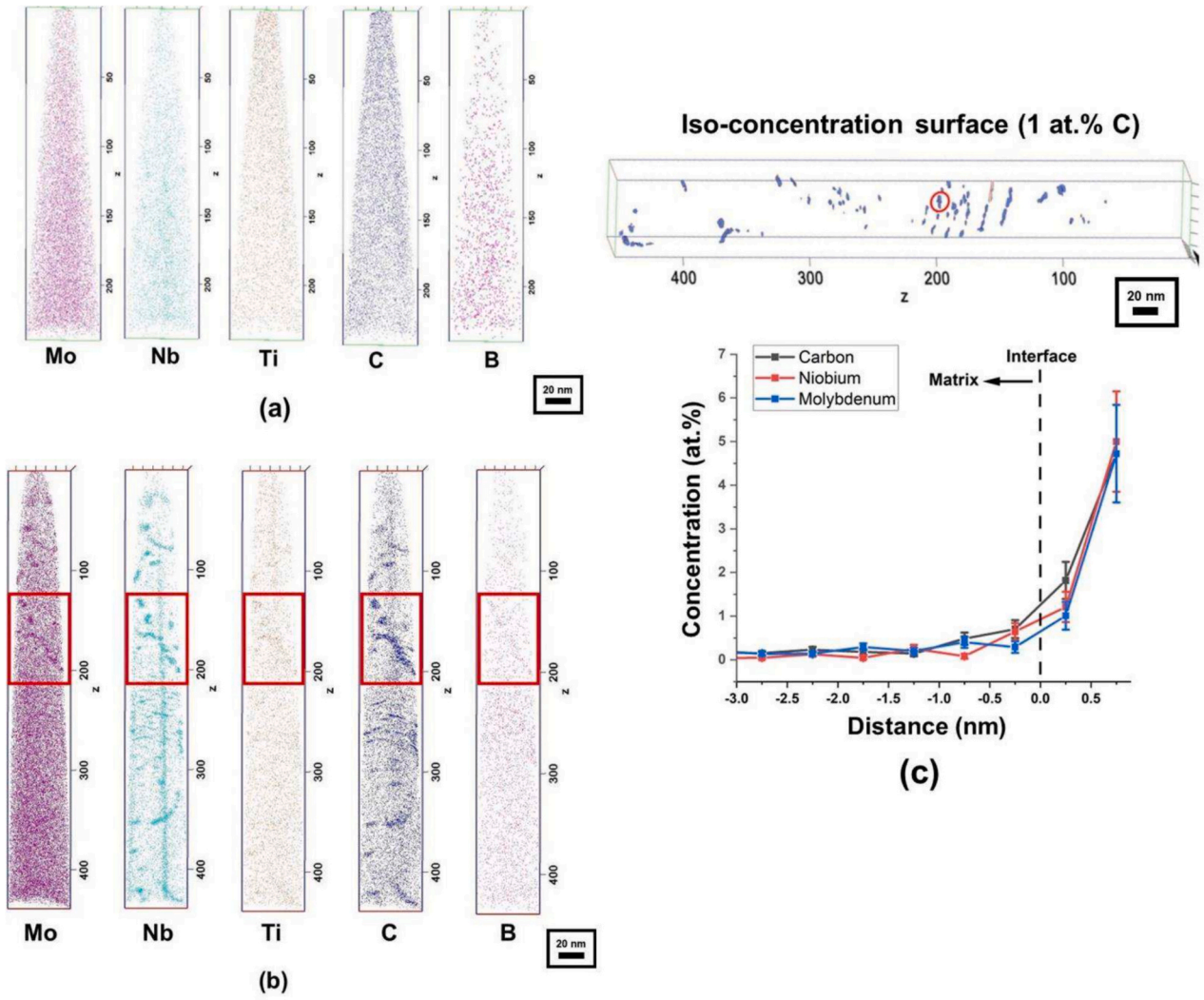

Fig. 5. Atom probe tomography results. (a) Atom maps for the as-received condition; (b) Atom maps for the fire-simulated condition; (c) Proxigram profile for the selected interface (red circle) with isoconcentration surface of 1 at. % C for fire-simulated condition. (For interpretation of the references to color in this figure legend, the reader is referred to the web version of this article.)

the primary effect of B in enhancing fire resistance is attributed to the possible segregation of B at the interfaces between NbC-type nanoprecipitates and the ferritic matrix. This segregation is believed to hinder the movement of interfaces during high-temperature testing, thereby slowing the coarsening kinetics of both the nanoprecipitates and the grains.

4.3. Alloying elements effect, and nanoprecipitates formation in dislocations and subgrains

In the development of this new fire-resistant steel alloyed with Nb, Mo, B, Ti, and C, significant emphasis has been placed on both the individual and synergistic contributions of these elements. Through TMCP and strategic alloying, this study aimed to optimize the microstructural stability and mechanical properties at elevated temperatures essential for fire resistance. Individual contributions of the elements include Nb and Ti, known for their strong carbide-forming tendencies, which lead to the formation of NbC and (Nb, Ti)C precipitates as observed in the TEM analysis. These precipitates significantly contribute to the strength and stability of the steel at high temperatures by hindering grain growth and promoting fine grain structures, thereby reducing dislocation mobility and maintaining strength under thermal stress. Molybdenum enhances high-temperature mechanical properties through solid solution strengthening and carbide refinement, improving resistance to overaging at elevated temperatures. Boron segregated to phase boundaries may prevent grain coarsening at high temperatures and hinder the coarsening of NbC precipitates, while C, the primary interstitial element, forms stable carbides with Nb and Ti, essential for maintaining structural stability during fire exposure.

In this study, thermodynamic predictions indicated the formation of NbC precipitates in the as-received condition, a result that was corroborated by SEM and TEM analyses. These techniques confirmed the presence of NbC-type precipitates within the microstructure, as illustrated in Figs. 3 and 4. However, our APT results did not detect these precipitates in the analyzed samples. This discrepancy can be attributed to several factors that influence the formation and stability of NbC precipitates. Firstly, the kinetic factors such as cooling rates and local compositional fluctuations play a significant role in precipitate formation. The cooling rate after thermomechanical processing can affect the nucleation and growth of precipitates, potentially leading to variations in precipitate distribution within the microstructure. Additionally, the presence of other alloying elements such as Mo and Ti may influence the stability and formation of NbC by altering the local chemical environment, thereby affecting the thermodynamic and kinetic pathways for precipitate formation. Processing conditions, including the specifics of the thermomechanical treatment and the environmental conditions

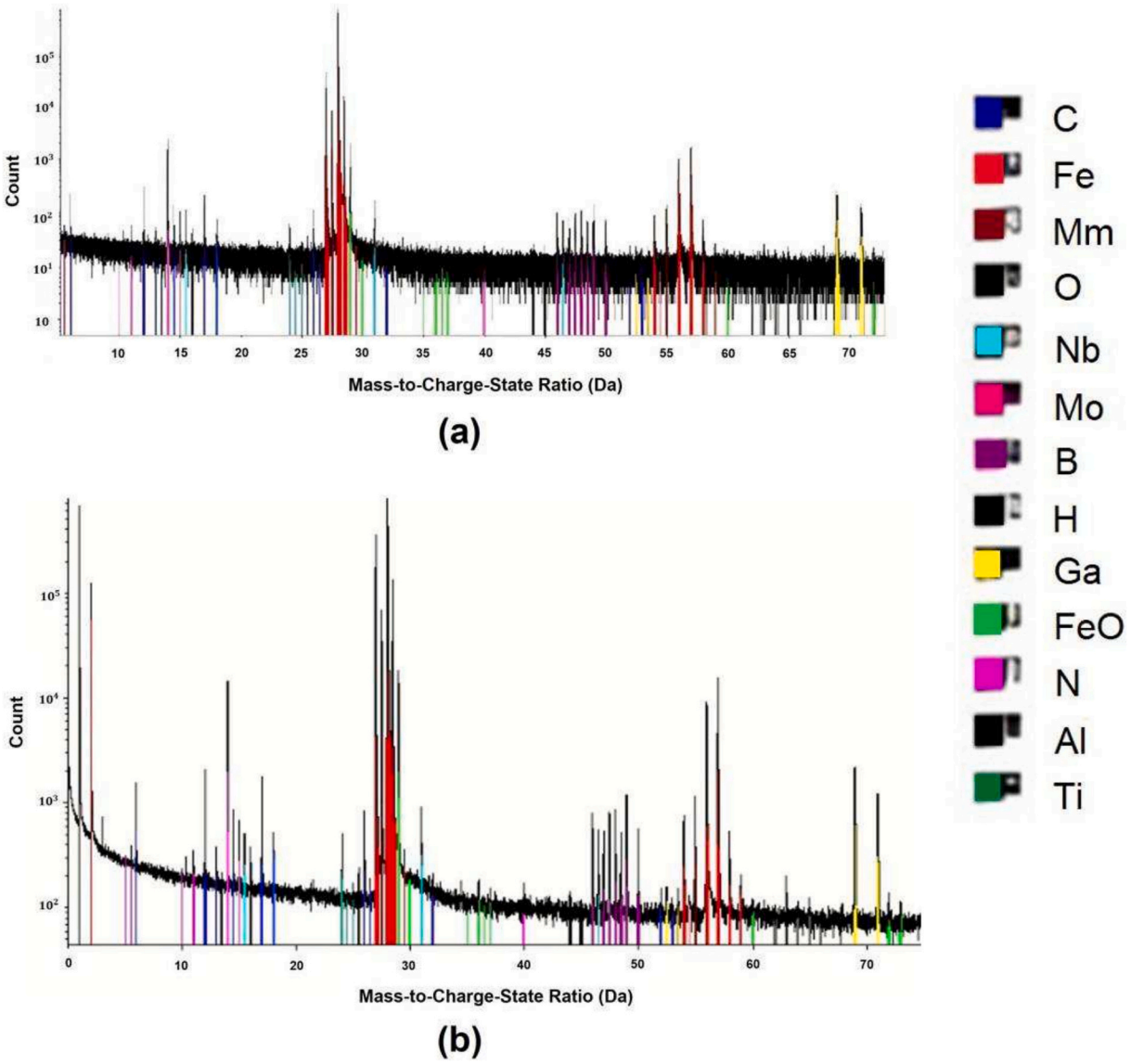

Fig. 6. Representative mass-to-charge-state spectra obtained by APT for the fire-resistant steel under two conditions: (a) as-received and (b) fire-simulated. The spectra show characteristic peaks for the primary elements detected, including Fe, C, Nb, Mo, Ti, and B, as well as trace Ga from FIB-SEM preparation.

during cooling, also critically impact the microstructure.

Additionally, TEM-EDS mapping indicates that Ti and Mo atoms interact with NbC nanocarbides, while atomic maps reveal that Mo and B atoms are also associated with NbC nanocarbides. The size of the nanoprecipitates found in the fire-simulated condition can impose additional barriers for the dislocation slip, delaying the kinetics of softening mechanisms, such as recovery and grain growth [29]. The increase in temperature also contributes to diffusion mechanisms of the atoms present in the clusters, which migrate to dislocation lines, being able to pin dislocation sliding and retarding the kinetics of softening mechanisms [29,30].

Ali et al. [31] studied the impact of adding B and Nb to low-carbon steels. The authors showed that the increase in the B content influences the formation of coarse precipitates $M_{23}(B, C)_6$ type, which precipitate in the previous austenitic grain boundaries (PAGB), reducing the steel hardenability and fracture toughness. Furthermore, the authors reported the synergistic effect between Nb + B: the presence of Nb in solid solution can prevent the precipitation of $M_{23}(B, C)_6$, where (M = Fe, Cr) in the PAGB, therefore combining with C atoms to form NbC or Nb(C, N). Sharma, Ortlepp, and Bleck [27] emphasized that B can form complex precipitates (B_2O_3, BN, $M_{23}(B, C)_6$, $M_7(B, C)_3$).

In this study, the presence of B in a solid solution was indicated, as shown in Fig. 5(a) for the "as-received" condition. When subjected to FS conditions, the atomic maps, as depicted in Fig. 5(b), revealed the presence of B atoms in regions rich in NbC nanoprecipitates.

The designed alloy demonstrated superior performance compared to standard Mo microalloyed fire-resistant steels, which typically show reduced efficacy at elevated temperatures due to rapid grain growth and precipitate coarsening. The refined microstructure and effective distribution of stable carbides, facilitated by the strategic use of Nb, Ti, B, and Mo, allow this alloy to maintain higher yield strength ratios and exhibit less structural degradation at 600 °C, surpassing the benchmarks set by existing solutions as required by the ASTM and Japanese codes. This highlights the importance of understanding how each alloying element and its interaction can contribute to enhanced fire resistance, providing valuable insights into the design of advanced fire-resistant steels capable of meeting the rigorous demands of safety and performance in structural applications.

4.4. Correlation between mechanical properties and microstructure

It is known that the mechanical properties of steel change drastically

under high temperatures, which is detrimental to structural parts that must withstand high temperatures. Dere et al. [13] highlight some softening mechanisms that reduce the strength of steel under fire conditions: (1) increased movement of dislocations, reducing the dislocation density present in the matrix by recovery processes [29]; (2) grain growth and precipitate coarsening; (3) phase transformation, depending on temperature range and chemical composition; (4) sliding of grain boundaries (creeping effect). Many articles [8,10,32] emphasize the effects of vacancy diffusion, which increases exponentially with increasing temperature.

In the present work, some characteristics of the microstructure were observed that are related to the signs of degradation of the microstructure, such as the decomposition of the MA microconstituent and the formation of secondary nanoprecipitates, which can suffer coarsening in prolonged fire exposure times, decreasing the hardening effect via precipitates dispersion. On the other hand, the fire-simulated microstructure showed a microstructural stability evidenced by its similarity with the as-received microstructure.

In the work published by Walp [9], except for the Cu and Ni-related FRS studied separately, the highest ratio $\frac{YS(600^{\circ}C)}{YS\ RT}$ was found for the alloy 0.48 Mo + 0.017 Nb (wt%), which achieved a ratio of 0.83. The author attributed the result to the additions of Mo + Nb, which synergistically act to retard Fe diffusion within the crystalline lattice, thereby promoting the formation of finer grains and microconstituents compared to other alloys studied.

Jo et al. [8] also found the best ratio $\frac{YS(600^{\circ}C)}{YS\ RT}$ for the Mo + Nb alloy. However, the authors reduced the Mo content to 0.30 wt% and increased the Nb content to 0.048 %, achieving a ratio of 0.79. Moon et al. [16] found the best ratio $\frac{YS(600^{\circ}C)}{YS\ RT}$ for the alloy containing 0.10 % C + 0.15 % Mo + 0.03 % Nb, reaching a ratio of 0.72. In the present study, it was shown that by reducing the Mo content to 0.25 % and adding 0.10 % Nb + 30 ppm B, it was possible to obtain the ratio $\frac{YS(600^{\circ}C)}{YS\ RT}$ of 0.76.

5. Conclusions

Based on the results obtained, it was concluded that:

- The primary precipitation of complex carbides (Nb, Ti, Mo)C, approximately 20 nm in size, was identified in the as-received condition, evidencing the effective action of these elements in microstructure stabilization. In the fire-simulated condition, secondary nanoprecipitates of (Nb, Ti)C, approximately 10 nm, were observed, highlighting the resilience of the microstructure under high-temperature conditions.
- In the fire-simulated condition, NbC nanoprecipitates were evident at dislocations or subgrain structures, indicating their role in hindering dislocation movement and enhancing high-temperature stability.
- The observations from APT underline the crucial interaction between Nb, C, Mo, Ti, and B. This synergy is important in forming and stabilizing NbC nanoprecipitates, which significantly contribute to the microstructural integrity and thermal stability of the steel. Particularly, the segregation of Mo within the NbC-type nanoprecipitates suggests a mechanism for refining these precipitates, thus enhancing their effectiveness at high temperatures.
- The combined effect of the alloying elements not only stabilizes the microstructure but also optimally enhances the material's fire resistance properties. The observed YS ratio of 0.76 at 600 °C compared to room temperature exceeds the stringent requirements specified in the Japanese Code, demonstrating the alloy's superior performance.
- These findings confirm that the strategic use of Nb, Ti, Mo, and B, in conjunction with the thermomechanical processing applied plays an important role in developing a fire-resistant steel that not only meets but surpasses current performance benchmarks for high-temperature applications. The study illustrates the effectiveness of this alloy composition in providing enhanced fire resistance through microstructural stability and precipitation refinement mechanisms.

CRediT authorship contribution statement

L.F. Bauri: Writing – original draft, Validation, Resources, Investigation, Formal analysis, Conceptualization. **A.M. Ferreira:** Software, Methodology, Investigation, Data curation. **E.A. Ariza-Echeverri:** Writing – original draft, Validation, Resources, Investigation, Formal analysis, APT analysis. **F.M.S.B. Carvalho:** Project administration, Funding acquisition, Formal analysis, Conceptualization. **P.M.C.D. Gomes:** Formal analysis, Conceptualization. **R. Sonkusare:** Validation, Software, Methodology, Investigation, Formal analysis, Data curation. **Y. Lu:** Software, Investigation, Formal analysis, Data curation. **T. Boll:** Validation, Supervision, Software, Resources, Project administration, Investigation, Funding acquisition, Formal analysis, Data curation. **A.P. Tschiptschin:** Supervision, Resources, Project administration, Methodology, Funding acquisition, Formal analysis, Data curation, Conceptualization. **H. Goldenstein:** Writing – original draft, Visualization, Validation, Supervision, Resources, Project administration, Methodology, Investigation, Funding acquisition, Formal analysis, Data curation, Conceptualization.

Declaration of competing interest

We have no conflicts of interest to disclose.

Acknowledgments

This research work has been supported by Companhia Brasileira de Metalurgia e Mineração (CBMM) and Empresa Brasileira de Pesquisa e Inovação Industrial – EMBRAPII MCE Contract 19.5.02.

We also gratefully acknowledge the financial support of the Coordenação de Aperfeiçoamento de Pessoal de Nível Superior (CAPES).

The authors acknowledge the Technological Research Institute (IPT) of São Paulo for providing the thermomechanically processed samples. We extend our heartfelt thanks to Dr. Ana Paola Villalva Braga and Dr. Mario Boccalini Jr. of IPT for their invaluable contributions and insightful discussions throughout the course of this project.

The authors would like to thank the Karlsruhe Institute of Technology (KIT) for the partnership and assistance in the TEM and APT analysis and Marina Weinhard during the period spent in Germany (Proposal number: KNMF 2021-026-030541), and post-stay discussions.

Data availability

No data was used for the research described in the article.

References

[1] S.S. Sunder, R.G. Gann, W.L. Grosshandler, H.S. Lew, R.W. Bukowski, F. Sadek, F. W. Gayle, J.L. Gross, T.P. McAllister, J.D. Averill, J.R. Lawson, H.E. Nelson, S. A. Cauffman, Final Report on the Collapse of the World Trade Center Towers, Gaithersburg, MD, 2005, https://doi.org/10.6028/NIST.NCSTAR.1.

[2] S.P. Chiew, M.S. Zhao, C.K. Lee, Mechanical properties of heat-treated high strength steel under fire/post-fire conditions, J. Constr. Steel Res. 98 (2014) 12–19, https://doi.org/10.1016/j.jcsr.2014.02.003.

[3] Z. Xie, Z. Song, K. Chen, M. Jiang, Y. Tao, X. Wang, C. Shang, Study of nanometer-sized precipitation and properties of fire resistant hot-rolled steel, Metals (Basel) 9 (2019) 1230, https://doi.org/10.3390/met9111230.

[4] Z. Zhang, Q. Yong, X. Sun, Z. Li, J. Kang, G. Wang, Microstructure and mechanical properties of precipitation strengthened fire resistant steel containing high Nb and low Mo, J. Iron Steel Res. Int. 22 (2015) 337–343, https://doi.org/10.1016/S1006-706X(15)30009-1.

[5] M. Maslak, R. Skiba, Fire resistance increase of structural steel through the modification of its chemical composition, Proc. Eng. 108 (2015) 277–284, https://doi.org/10.1016/j.proeng.2015.06.148.

[6] R. Wan, F. Sun, L. Zhang, A. Shan, Development and study of high-strength low-Mo fire-resistant steel, Mater. Des. 36 (2012) 227–232, https://doi.org/10.1016/j.matdes.2011.10.055.
[7] H.H. Wang, Z.P. Qin, R. Wei, X.L. Wan, K.M. Wu, R.D.K. Misra, Precipitation of carbonitrides and high-temperature strength in heat-affected zone of high-Nb containing fire-resistant steel, Sci. Technol. Weld. Join. 22 (2017) 157–165, https://doi.org/10.1080/13621718.2016.1207288.
[8] H.H. Jo, C. Shin, J. Moon, J.H. Jang, H.Y. Ha, S.J. Park, T.H. Lee, B.H. Lee, J. H. Chung, J.G. Speer, K.O. Findley, T.R. Jacobs, C.H. Lee, S.D. Kim, Mechanisms for improving tensile properties at elevated temperature in fire-resistant steel with Mo and Nb, Mater. Des. 194 (2020) 108882, https://doi.org/10.1016/j.matdes.2020.108882.
[9] M. Walp, Fire-Resistant Steels for Construction Applications, Colorado School of Mines, 2003.
[10] P.P. Ferreira, F.M. Carvalho, E.A. Ariza-Echeverri, P.M. Delfino, L.F. Bauri, A. M. Ferreira, A.P. Braga, L.T.F. Eleno, H. Goldenstein, A.P. Tschiptschin, Synergism between B and Nb improves fire resistance in microalloyed steels, Metals (Basel) 13 (2023) 84, https://doi.org/10.3390/met13010084.
[11] J.D. Escobar, P.M. Delfino, E.A. Ariza-Echeverri, F.M. Carvalho, N. Schell, A. Stark, T.A. Rodrigues, J.P. Oliveira, J.A. Avila, H. Goldenstein, A.P. Tschiptschin, Response of ferrite, bainite, martensite, and retained austenite to a fire cycle in a fire-resistant steel, Mater. Charact. 182 (2021) 111567, https://doi.org/10.1016/j.matchar.2021.111567.
[12] J. Cong, J. Li, J. Fan, R.D.K. Misra, X. Xu, X. Wang, Effect of austenitic state before ferrite transformation on the mechanical behavior at an elevated temperature for seismic-resistant and fire-resistant constructional steel, J. Mater. Res. Technol. 13 (2021) 1220–1229, https://doi.org/10.1016/j.jmrt.2021.05.061.
[13] E.G. Dere, H. Sharma, R.H. Petrov, J. Sietsma, S.E. Offerman, Effect of niobium and grain boundary density on the fire resistance of Fe-C-Mn steel, Scr. Mater. 68 (2013) 651–654, https://doi.org/10.1016/j.scriptamat.2012.12.030.
[14] R. Chijiiwa, H. Tamehiro, R. Uemori, Y. Horii, Y. Yoshida, K. Funato, Development and practical application of fire-resistant steel for buildings, in: SEAISI Quarterly (South East Asia Iron and Steel Institute), Publ by Nippon Steel Corp, 1994, pp. 55–66.
[15] L.J. Wei, Y.S. Yu, T.Z. Lin, Z.Q. Wang, P.C. Liu, R.D.K. Misra, X.M. Wang, New insights into the contribution of grain boundaries on fire resistance of 690 MPa ultra-heavy plate steel, Mater. Lett. 295 (2021) 129805, https://doi.org/10.1016/j.matlet.2021.129805.
[16] J. Moon, S.-D. Kim, C.-H. Lee, H.-H. Jo, H.-U. Hong, J.-H. Chung, B.H. Lee, Strengthening mechanisms of solid solution and precipitation at elevated temperature in fire-resistant steels and the effects of Mo and Nb addition, J. Mater. Res. Technol. 15 (2021) 5095–5105, https://doi.org/10.1016/j.jmrt.2021.10.132.
[17] H. Mohrbacher, Principal Effects of Mo in HSLA Steels and Cross Effects With Microalloying Elements for International Seminar in Applications of Mo in Steels 13, Central Iron and Steel Research Institute (CISRI), 2010, pp. 75–96.
[18] R. Chijiiwa, H. Tamehiro, Y. Yoshida, K. Funato, R. Uemori, Y. Horii, Development and Practical Application of Fire-Resistant Steel for Buildings, Nippon Steel Technical Report No. 58, 1993, pp. 47–55.
[19] L.J. Wei, X.M. Ji, Y.S. Yu, R.D.K. Misra, P.C. Liu, X.M. Wang, Retained austenite-induced fire-resistance of a 690 MPa high strength steel, Mater. Lett. 291 (2021), https://doi.org/10.1016/j.matlet.2021.129448.
[20] ASTM, ASTM E8: Standard Test Methods for Tension Testing of Metallic Materials, 2001.
[21] ASTM E21-17, Standard Test Methods for Elevated Temperature Tension Tests of Metallic Materials, ASTM 03, 2019, pp. 1–8.
[22] P.M.C.D. Gomes, Transformações de Fase, Microestruturas, e Propriedades Mecânicas de um aço Resistente ao Incêndio, Universidade de São Paulo (USP), 2022. https://www.teses.usp.br/teses/disponiveis/3/3133/tde-04032022-113948/publico/PedroMeirellesChagasDelfinoGomesCorr22.pdf. (Accessed 6 October 2023).
[23] E119 - Standard Test Methods for Fire Tests of Building Construction and Materials, Philadelphia, PA, USA, 1996.
[24] W. Sha, F.S. Kelly, Z.X. Guo, Microstructure and properties of nippon fire-resistant steels, J. Mater. Eng. Perform. 8 (1999) 606–612, https://doi.org/10.1007/s11665-999-0017-3.
[25] R.W.K. Honeycombe, H.K.D.H. Bhadeshia, Steels: Microstructure and Properties, Butterworth-Heinemann, 2017.
[26] R. Wan, F. Sun, L. Zhang, A. Shan, Effects of Mo on high-temperature strength of fire-resistant steel, Mater. Des. 35 (2012) 335–341, https://doi.org/10.1016/j.matdes.2011.09.009.
[27] M. Sharma, I. Ortlepp, W. Bleck, Boron in heat-treatable steels: a review, Steel Res. Int. 90 (2019) 1900133, https://doi.org/10.1002/srin.201900133.
[28] A.M. Ferreira, E.A. Ariza, L.F. Bauri, P.M.C.D. Gomes, F.M.S.B. Carvalho, M. Masoumi, J.D. Poplawsky, H. Goldenstein, A.P. Tschiptschin, A new strategy for developing a Nb microalloyed fire-resistant steel: effects of boron and cooling rate, J. Mater. Res. Technol. 33 (2024) 2365–2376, https://doi.org/10.1016/j.jmrt.2024.09.150.
[29] A. Rollett, F. Humphreys, G.S. Rohrer, M. Hatherly, Recrystallization and Related Annealing Phenomena, Second edition, Elsevier, 2004, https://doi.org/10.1016/B978-0-08-044164-1.X5000-2.
[30] A.W. Cochardt, G. Schoek, H. Wiedersich, Interaction between dislocations and interstitial atoms in body-centered cubic metals, Acta Metall. 3 (1955) 533–537, https://doi.org/10.1016/0001-6160(55)90111-5.
[31] M. Ali, T. Nyo, A. Kaijalainen, V. Javaheri, H. Tervo, J. Hannula, M. Somani, J. Kömi, Incompatible effects of B and B + Nb additions and inclusions' characteristics on the microstructures and mechanical properties of low-carbon steels, Mater. Sci. Eng. A 819 (2021) 141453, https://doi.org/10.1016/j.msea.2021.141453.
[32] R. Idczak, R. Konieczny, Behaviour of vacancies in dilute Fe–re alloys: a positron annihilation study, Appl. Phys. A 117 (2014) 1785–1789, https://doi.org/10.1007/s00339-014-8830-4.